Additive Manufacturing 36 (2020) 101426

Contents lists available at ScienceDirect

Additive Manufacturing

journal homepage: www.elsevier.com/locate/addma

Effect of build thickness and geometry on quasi-static and fatigue behavior of Ti-6Al-4V produced by Electron Beam Melting

S.M.J. Razavi[a,*], B. Van Hooreweder[b], F. Berto[a]

[a] Norwegian University of Science and Technology (NTNU), Department of Mechanical and Industrial Engineering, Richard Birkelands Vei 2b, 7491 Trondheim, Norway
[b] KU Leuven, Department of Mechanical Engineering, Celestijnenlaan 300b – B3001 Leuven, Belgium

ARTICLE INFO

Keywords:
Build thickness
Electron beam melting
Geometry effect
Size effect
Ti-6Al-4V

ABSTRACT

The geometry and material properties of additively manufactured (AM) parts are closely related in a way that any alteration in geometry of the part will change the underlying manufacturing strategy. This in turn, affects the microstructure and consequently, the mechanical behavior of material. This paper aims to evaluate the effect of the AM part's thickness and geometry on microstructure, surface roughness, and mechanical properties under quasi-static and fatigue loading conditions by performing experimental tests. A series of Ti-6Al-4V specimens with three different thicknesses and two different geometries were fabricated using electron beam melting (EBM). The results of microstructural analyses revealed that specimens with lower build thickness experience finer grain size, higher microhardness, and lower elongation at failure. Although the microstructure of the produced parts was strongly affected by the build thickness, different surface to volume ratios eliminated the effect of microstructural differences and governed the fatigue properties of the parts. The size effect on the microstructural features, geometrical appearance, mechanical properties of the AM parts should be considered for the design and failure analysis of complex structures.

1. Introduction

Additive Manufacturing (AM) technology allows direct conversion of digital unprecedented complex designs into physical products within one completely autonomous production step while avoiding setup time and the use of tools. This technology has significantly evolved, from prototyping to production and repairing of functional industrial parts for service [1–3]. Despite the ability of AM technology in fabrication of geometrically complex components, the material properties of the produced AM parts are closely associated with the input geometry. Different geometries or scales of the given geometry change the way that the AM machine performs its building routine, affecting the printing strategy and, ultimately, the microstructure and mechanical properties of the resulting solid [4]. On the other hand, depending on the underlying manufacturing strategy, anisotropy, presence of residual stresses, geometrical imperfections, and poor surface conditions are commonly reported for AM parts, which can be largely eliminated using different post-processing techniques [5–9]. For metals, two main categories of AM technologies have been developed, namely Powder Bed Fusion (PBF) [10] (e.g. Selective Laser Melting (SLM), Direct Metal Laser Sintering (DMLS), and Electron Beam Melting (EBM)) and Direct Energy Deposition (DED) [11] (e.g. Laser Engineered Net Shaping (LENS), Directed Light Fabrication (DLF), Direct Metal Deposition (DMD), and Laser Cladding (LC)).

The Electron Beam Melting (EBM) technique developed by Arcam employs an electron beam as energy source to melt the metal powder in a high vacuum chamber at elevated temperatures (~650−700 °C) to preserve the chemical characteristics of the build material and to produce components with negligible residual stresses and free from martensite phases [12]. The components produced by EBM are currently being used in orthopedic implants, aerospace parts, marine applications, and gas turbines [13,14]. The standard materials produced by EBM are titanium alloy Ti-6Al-4V, titanium alloy Ti-6Al-4V ELI, titanium grade 2, ASRM F75 cobalt-chrome, and Inconel 718; among which, Ti-6Al-4V has been widely used due to its high specific strength, fatigue strength, and corrosion resistance. The EBM Ti-6Al-4V parts were reported to have fine needle-like α phase separated by the β phase [12,15–17], resulting in superior static tensile properties compared to the cast material and comparable properties with the wrought ones [18]. Unlike the common fully martensitic microstructure of Ti-6Al-4V parts printed by laser PBF technologies, where a standard heat treatment is commonly required to reach the proper microstructure and mechanical properties [19], the EBM parts usually have fine α + β microstructure (e.g., colony and basket-weave morphology), which

* Corresponding author.
E-mail address: javad.razavi@ntnu.no (S.M.J. Razavi).

https://doi.org/10.1016/j.addma.2020.101426
Received 19 November 2019; Received in revised form 25 June 2020; Accepted 26 June 2020
Available online 29 June 2020

results in the superior mechanical properties of these parts. In this case, performing standard heat treatments such as sub-β-transus or super β-trans does not significantly improve the mechanical properties [20]. Numerous studies have been performed on the effect of process parameters [21] and geometrical aspects of the printed part (such as height [18,22] and thickness [22–26]) on the microstructural features of EBM Ti-6Al-4V. The previous studies on the build thickness dependent microstructure of EBM Ti-6Al-4V show that higher simulated temperature profile in thicker EBM samples compared to the thin samples results in larger grain size [22–26]. In recent research on the EBM-built Ti-6Al-4V turbine component, Wang et al. [27] reported that a finer microstructure exists in the blade region as compared to the block region of the turbine due to higher cooling rate attributed to lower thermal input in this thin region.

Since the AM technology is commonly being employed for the fabrication of complex geometries, an essential task would be to study the sensitivity of the printed material to the presence of geometrical discontinuities in the design. Some recently published works have studied the notch fatigue behavior of AM Ti-6Al-4V by considering the effect of surface roughness and internal defects of the test specimens and by correlating these two with the final fatigue life of the tested specimens [28–32].

Generally speaking, the knowledge and prediction of the overall mechanical performance of EBM parts still encounter scrutiny and will depend on various factors such as the microstructure of printed material, surface condition, and statistics of the internal defects. These factors are thought to be dependent on the input geometry of the part. In the design of complex industrial and biomedical components, the presence of non-uniform section thickness and geometrical discontinuities such as notches are unavoidable. Consequently, the AM parts typically have a gradient of different microstructural features, surface roughness, and internal defects. To the best of authors' knowledge, the effect of geometry and size on the fatigue behavior of EBM has yet to be studied. Hence, this research aims to contribute to the fundamental understanding of the build thickness effect on microstructural features and mechanical performance of EBM Ti-6Al-4V specimens under quasi-static and fatigue loading conditions.

Two sets of specimens, namely unnotched and notched with three different thicknesses were considered for the experimental studies. Since the test specimens have different thicknesses, the in-fill hatching time would be different, resulting in different thermal histories and consequently different microstructures. In the first part of the article, the employed manufacturing process for the EBM specimens is described, followed by the resulting microstructures of specimens with different thicknesses. Lastly, the quasi-static and fatigue test results of unnotched and notched EBM specimens are presented, and the mechanical behaviors of different tested specimens are correlated to the microstructural features, and surface condition of the printed specimens.

2. Materials and methods

2.1. Specimens fabrication

The test specimens were fabricated in an Arcam Q20 with 3000 W maximum power of electron gun, hatch line offset of 220 μm, layer height of 90 μm, and two circumferential contours using gas atomized Ti-6Al-4V (grade 5) powder with a size distribution of 40–105 μm. Six different sets of test specimens with two plane geometries (i.e., unnotched and notched) and three different thicknesses were fabricated vertically (along Z axis). The schematic geometry of the test specimens is given in Fig. 1. No post-treatment, including heat treatment and surface treatment was performed on the EBM specimens.

2.2. Metallography

EBM samples were sectioned horizontally and vertically along the centerline to analyze the microstructure. The samples were then hot-mounted in PolyFast, ground (final grinding step: 4000 grit), polished using Akasel water-free polycrystalline diamond suspension (final polishing step: 0.25 μm), final polished using Struers 50 nm colloidal silica suspension, and etched using Kroll's reagent, an etching solution containing 3 mL HF, 6 mL HNO_3 and 100 mL distilled water (ASTM E407-07). After etching the Ti-6Al-4V samples with the mentioned etchant, the α grains would be revealed with bright color, while the β grains would have a darker shade under an optical microscope. The microstructures of the etched samples were observed using an optical microscope (Olympus, BX53MRF-S, Tokyo, Japan).

2.3. Surface roughness measurement

The surface morphology and roughness of specimens were evaluated using an Alicona Infinite Focus Microscope (IFM) (Graz, Austria). This non-contact microscope uses optical light as the medium for roughness measurements. The available objectives vary from 2.5× to 100× magnifications and a vertical resolution of up to 10 nm can be obtained at 100× magnification [33]. The surface analyses were performed by setting the proper parameters according to EN ISO 4287 standard. In order to evaluate the effect of overhang, in the notched specimens, two specimens were considered for each thickness and roughness measurements were carried out on three locations on the upward and downward faces of the notch together with the side surface of the specimens. The arithmetic average of the surface roughness profile, R_a, and maximum peak to valley height of the roughness profile, R_t, were obtained for each series. Additional scanning electron microscope (SEM) (FEI, Quanta™ 650 FEG, Oregon, USA) analyses were performed on the notched specimens to study their surface morphology.

2.4. Microhardness measurement

Microhardness tests were conducted by indenting polished cross-sections of the specimens using a load of 300gf and dwell time of 15 s using a Mitutoyo micro Vickers hardness tester (Kawasaki, Japan). In order to obtain the variation of the microhardness values along the thickness of the specimens, the indents were made along four parallel paths through the thickness from the surface towards the nominal mid thickness of the specimens.

2.5. Tensile strength test

Monotonic tensile tests were carried out on unnotched and notched specimens with three different thicknesses, each consisting of three specimens. The specimens were tested using an MTS landmark servo-hydraulic test machine (Minnesota, USA) with a load cell capacity of 50 kN at a displacement rate of 1 mm/min. The elongation of the test specimen during the test was measured using an MTS extensometer with gage length of 5 mm attached to the surface of the specimens.

2.6. Fatigue test and fractography analysis

Uniaxial fatigue tests were performed using the same test machine under load control with a frequency of 30 Hz and a loading ratio of $R = 0$. In order to obtain the stress-fatigue life diagrams of different EBM specimens, an average of twelve specimens was tested for each testing case. Specimens that withstood at 2×10^6 cycles were considered as run-out. Probability of failure bands of 10, 50, and 90 % were plotted to obtain the inverse slope, k and scatter index, T_σ (the ratio between the stress level corresponding to 10 % and 90 % of survival probability) of the fatigue data. SEM analysis was used to study the failure mechanisms of the material after testing.

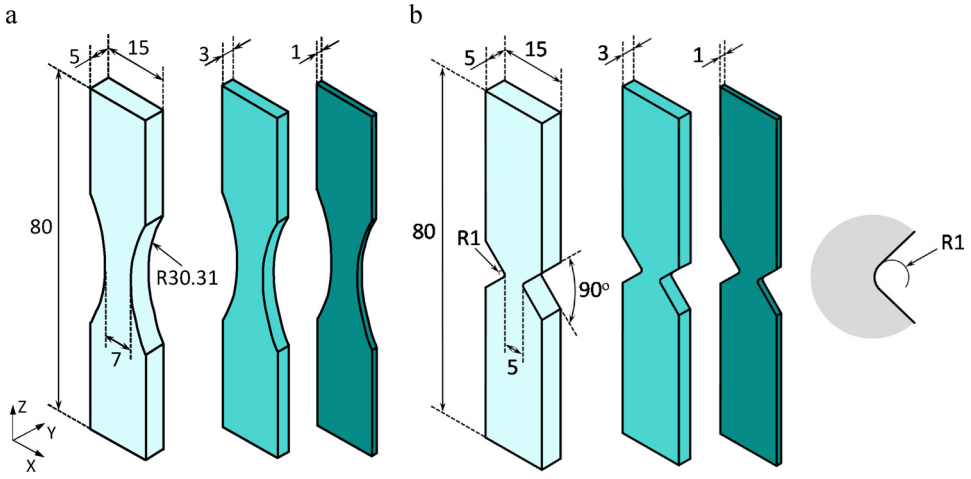

Fig. 1. Geometrical dimensions of the test specimens, (a) unnotched specimens, (b) notched specimens (unit: mm).

Considering the rough surface of as-built EBM specimens, the surface roughness introduces an error in calculation of section area of the specimen. Assuming a constant surface roughness for the specimens of different build thickness, the difference between the real applied stress and the nominal stress calculated based on design dimensions would increase by decreasing the build thickness resulting in higher applied stresses to the low thickness specimens. Special attention was paid in this research to present the quasi-static and fatigue properties based on real cross section of the specimens.

The SEM images were processed using ImageJ software to accurately measure the fracture surfaces of the failed specimens and therefore have a more precise measurement of the cross section for stress calculations. A representative illustration of the real cross section is provided as supplementary data. Alternative methods [34,35] have been used by researchers to calculate the load-bearing cross section area. It is worth mentioning that due to very high surface roughness of EBM specimens, the use of these techniques would eliminate a large portion of cross section resulting in unreasonably large tensile strengths.

3. Results

3.1. Microstructure

The microstructures of EBM samples in different longitudinal planes (i.e., XZ and YZ) and the transversal plane (i.e., XY) obtained from optical microscopy are shown in Fig. 2. The optical images in Fig. 2b and c illustrate the columnar microstructure of EBM samples with the prior beta grains elongated along the built direction. Higher magnitude observation in Fig. 3 reveals the notable inhomogeneous microstructure of EBM specimens. The three main microstructures, namely lamellar and basketweave $\alpha + \beta$ grains and equiaxed α grains were observed in the evaluated samples (see Fig. 3).

Fig. 4 displays a comparative view of different microstructures in the specimens with various thicknesses. Due to identical microstructures of notched and unnotched specimens of the same thickness in the net section, the presented results were chosen only from unnotched specimens. According to the optical images, the lamellar grains mainly exist around the boundary of the prior beta grains, while the basketweave and equiaxed grains were mostly observed in the inner region of the prior grains. By increasing the thickness of EBM specimens from 1 mm to 5 mm, the width and the length of α lamellae tend to increase. In this case, lamellar features were also observed among the basketweave microstructures. The same tendency was also observed for the equiaxed alfa grains within the parent grain. Following the thickness increase from 3 mm to 5 mm, larger microstructures were observed in thicker samples. In this case, the largest grains from optical images are illustrated in Fig. 4c. To better present the variation of microstructure size in different specimens, image analyses were performed on the obtained microstructures by use of ImageJ software and the width of the α lath were obtained from the analyses. The α lath width measurements supported the previous qualitative observation by revealing the median values of 1.9, 1.3, and 0.7 μm for the α lath width in the specimens with 5, 3 and 1 mm build thickness.

3.2. Surface roughness

Due to direct use of AM parts in some fields, such as biomedical applications, these parts are mostly used with as-built condition. The rough surface of the EBM specimen facilitates the bone growth and would result in better acceptance of the prosthesis by human body. It is then of great importance to explore whether the build thickness or the geometry of the part has an impact on the roughness and geometrical appearance of the resulting part.

The surface morphology of the upward, notch root, and downward faces of the notched specimens were evaluated using SEM. Fig. 5 represents different faces of the notched region in a specimen with 3 mm thickness. Downward face (also known as overhang face) refers to diagonal surfaces having the vertical component of the surface normal in the opposite direction of the build direction. While upward face refers to surfaces where the vertical component of the surface normal is in the same direction as the build progression. A comparative illustration of the surface condition in notched specimens with different build thicknesses is shown in Fig. 6.

Fig. 7 represents the surface roughness values obtained from the notched specimens with different build thicknesses. According to the surface morphology and surface roughness results, increasing the build thickness of the specimens resulted in lower surface roughness on the three studied faces. Unlike the apparent trend of roughness variation between different specimens, the downward surface of specimens with 1 mm build thickness showed lower surface roughness value compared to the other geometries and other faces of the same specimen. For the specimens with 3 mm and 5 mm build thickness, the downward faces had the highest R_t and a higher number of partially fused powder particles compared to the upward faces, which can affect the geometry of micro-notches on the surface. This high surface roughness on the downward faces may have limited effect on the failure location of the notched specimens in this research. However, in specific cases where the global notch induces lower stress concentration, the presence of deep micro-notches on the notch faces can result in unexpected failure from the notch faces instead of the notch root. The average surface roughness values of the EBM notch specimens are presented in Table 1.

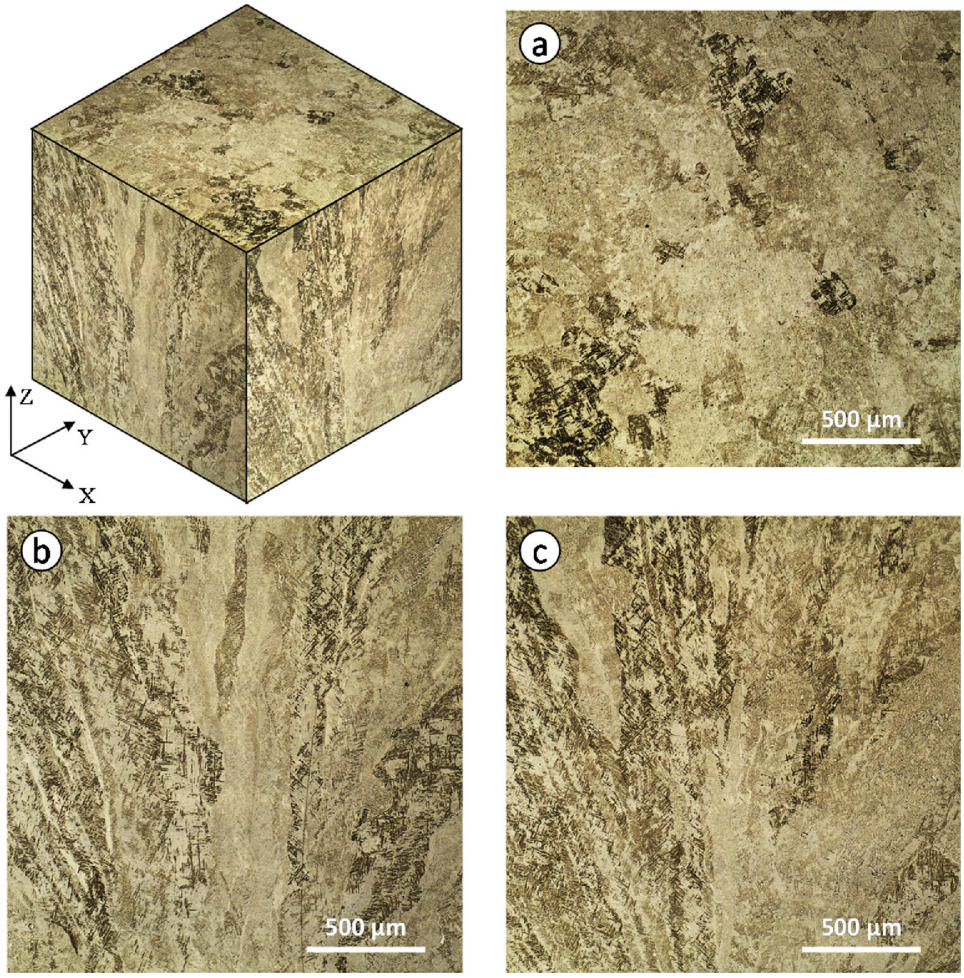

Fig. 2. Microstructure pattern of columnar prior β grains in different sections perpendicular (a) and parallel (b,c) to the build direction (Z axis).

3.3. Microhardness

The results of microhardness tests are presented in Fig. 8 for the specimens printed with different thicknesses. According to the experimental data, the EBM samples represent an almost constant trend of microhardness through the depth with an average microhardness value of 413, 391, and 386 for the specimens with 1, 3, and 5 mm thickness, respectively. The microhardness values of the evaluated samples are thought to be directly related to the size of microstructural features resulting in the highest microhardness value for the 1 mm samples with the finest grain size [36]. It is worth mentioning that all EBM samples exhibited higher microhardness values compared to Ti-6Al-4V manufactured by conventional techniques having a microhardness of 358 [37] (respectively about 15 %, 9%, and 8% higher for the specimens with 1, 3, and 5 mm thickness).

3.4. Tensile test

Fig. 9 compares the representative stress-strain curves obtained from different series of test specimens. The average tensile properties of the three tested specimens for each case are presented in Table 2. The quasi-static test results of unnotched specimens confirm that the smaller build thickness results in considerably lower elongation at failure in addition to the slightly higher tensile strength of the part. This is in line with the available data in literature on tensile properties of EBM parts (see Table 3). It is worth mentioning that the tensile strengths of the tested specimens are in the same range as reported by Arcam company [45]. However, the value reported by Arcam for elongation at failure of EBM Ti-6Al-4V is only close to the specimens with build thickness of 5 mm.

The notched specimens experienced almost similar tensile behavior. In order to have a better understanding of the stress triaxiality effect in the notched specimens, a set of numerical analysis was conducted on the different unnotched and notched specimens. Details of the numerical analysis are presented in Appendix A. According to the numerical results, variation of build thickness in the unnotched specimens has no significant effect on the triaxiality value. In this case, maximum triaxiality values (obtained in the mid-thickness) of 0.333, 0.334, and 0.335 were obtained for the parts with 1, 3, and 5 mm thickness. However, a noticeable effect of build thickness on stress triaxiality was observed in the notched parts, having the lowest and highest values of 0.348 and 0.416 for 1 mm and 5 mm specimens. Fig. 10 illustrates the variation of stress triaxiality in the studied geometries. Due to the higher stress triaxiality value in the thicker specimens (approximately 20 %), the notch strengthening effect is significantly more pronounced in these cases resulting in higher increase of the failure loads and higher reduction of elongation at failure to a level close to the thin specimens with higher strength and lower elongation at failure.

3.5. Fatigue and notch sensitivity

The fatigue test data for EBM Ti-6Al-4V specimens produced with different thicknesses and geometries are presented in Fig. 11, and the detailed fatigue data together with stress concentration factor and notch reduction factor of each tested case are reported in Table 4. The fatigue strengths of unnotched specimens at 2×10^6 cycles were 152,

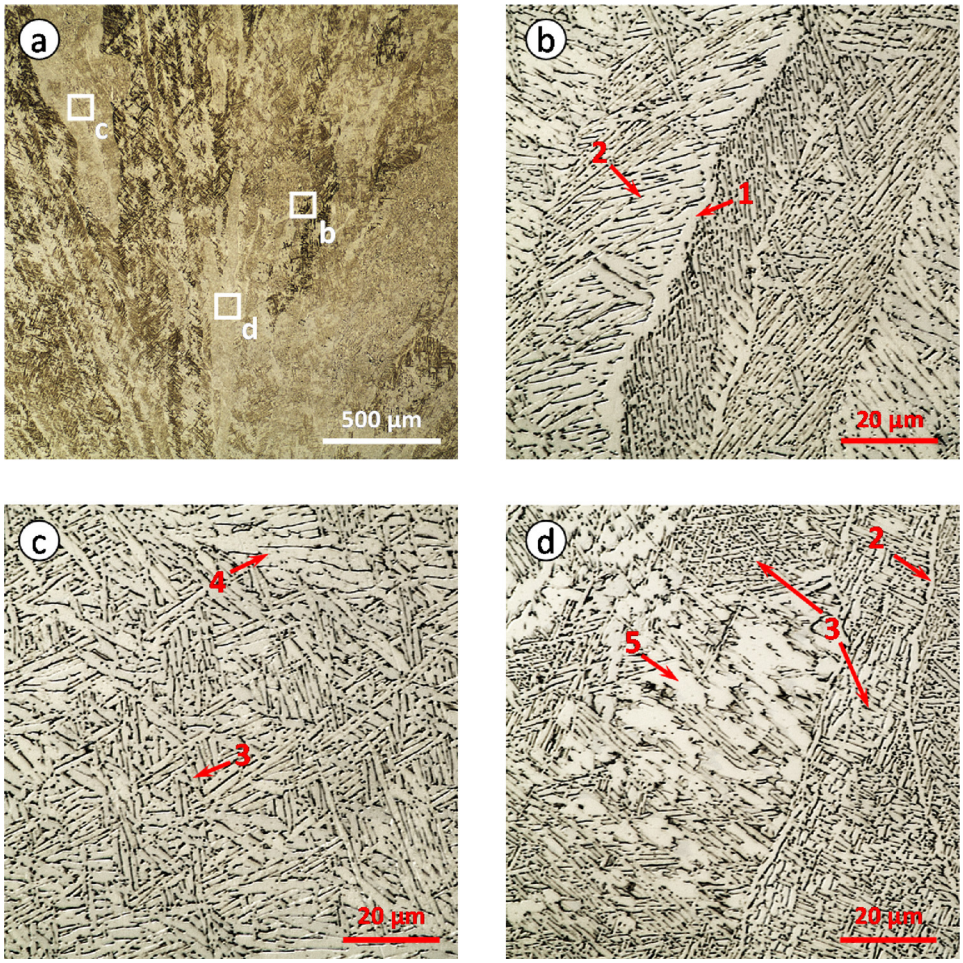

Fig. 3. Representative illustration of various microstructural features within the prior beta grains in the specimen with 3 mm thickness. The microstructural features are shown by number; (1) α layer formed at prior beta grain boundary, (2) α lamellae formed along the prior beta grain, (3) basketweave morphology including alfa colonies, (4) large α lamellae within the prior grain, (5) equiaxed alfa grains.

149, and 129 MPa for different thicknesses of 5, 3, and 1 mm. While in the case of notched specimens, fatigue strengths of 103, 101, and 85 MPa were obtained for 5, 3, and 1 mm thicknesses. As expected, the fatigue strengths of notched specimens were lower than those of unnotched specimens with the same thickness. In both cases, the fatigue strength was reduced by reducing the build thickness having the lowest value for 1 mm thick specimens.

According to the experimental data in Fig. 11 and Table 4, the scatter index, T_σ of the notched specimens is lower than the unnotched specimens with identical thickness. On the other hand, the specimens with 1 mm thickness have the highest scatter index, T_σ (1.38 for unnotched specimens, and 1.28 for notched specimens), while the scatter values of the specimens of 3 and 5 mm thickness with the same geometry were comparable. In all cases, as a result of presence of geometrical discontinuities the inverse slope of notched specimens were lower than that of the unnotched specimens, showing a steeper slope of S-N data.

The numerical results obtained from finite element analysis (as described in Appendix A) were used to calculate the stress concentration factors, K_t and eventually the notch sensitivity, q of the specimens. The stress concentration factor was considered as a ratio of maximum axial stress at the notch tip divided by the stress at net section. The K_t values obtained from mid-thickness of models are given in Table 4. The fatigue notch factor, K_f was experimentally obtained by diving the fatigue limit of unnotched specimens to that of the notched specimens (i.e. $K_f = \Delta\sigma_{50\%}|\ unnotched/\Delta\sigma_{50\%}|\ notched$). By substituting of the stress concentration factors and fatigue notch factors in $q = (K_f - 1)/(K_t - 1)$, the notch sensitivity can be calculated. According to this formula, $q = 1$ represents a material fully sensitive to presence of notch, while for a material insensitive to presence of notch, $q = 0$, giving $K_f = 1$ (i.e. $\Delta\sigma_{50\%}|\ unnotched = \Delta\sigma_{50\%}|\ notched$).

According to the experimental results, the specimens with 1 mm thickness experienced the highest notch sensitivity value of $q = 0.39$, which is slightly higher than the values obtained from the specimens of 3 and 5 mm thickness.

3.6. Fractography analysis

Fractography was performed on the fatigue tested specimens to evaluate possible differences in failure mechanisms between the specimens with different geometries. Fig. 12 represents the typical fracture surface resulted from fatigue failure of the part. Three distinct crack growth stages are indicated in Fig. 12, starting with the initial stable crack growth (shown with red arrow), quasi-stable crack growth (shown with white arrow), and final unstable crack growth followed by ductile failure (shown with black arrow). The fatigue cracks in EBM specimens were starting from the micro-notches on the surface (see Fig. 5) and propagating through the section of the specimens. Depending on the depth and the notch acuity of the micro-notch, the fatigue failure was starting from different locations along the specimens' surface. This stage of crack growth was identified by microstructural dependent micro features having a combination of intergranular and transgranular crack growth along the α + β grains (see Fig. 12b). These specific failure mechanisms resulted in a tortuous surface with an

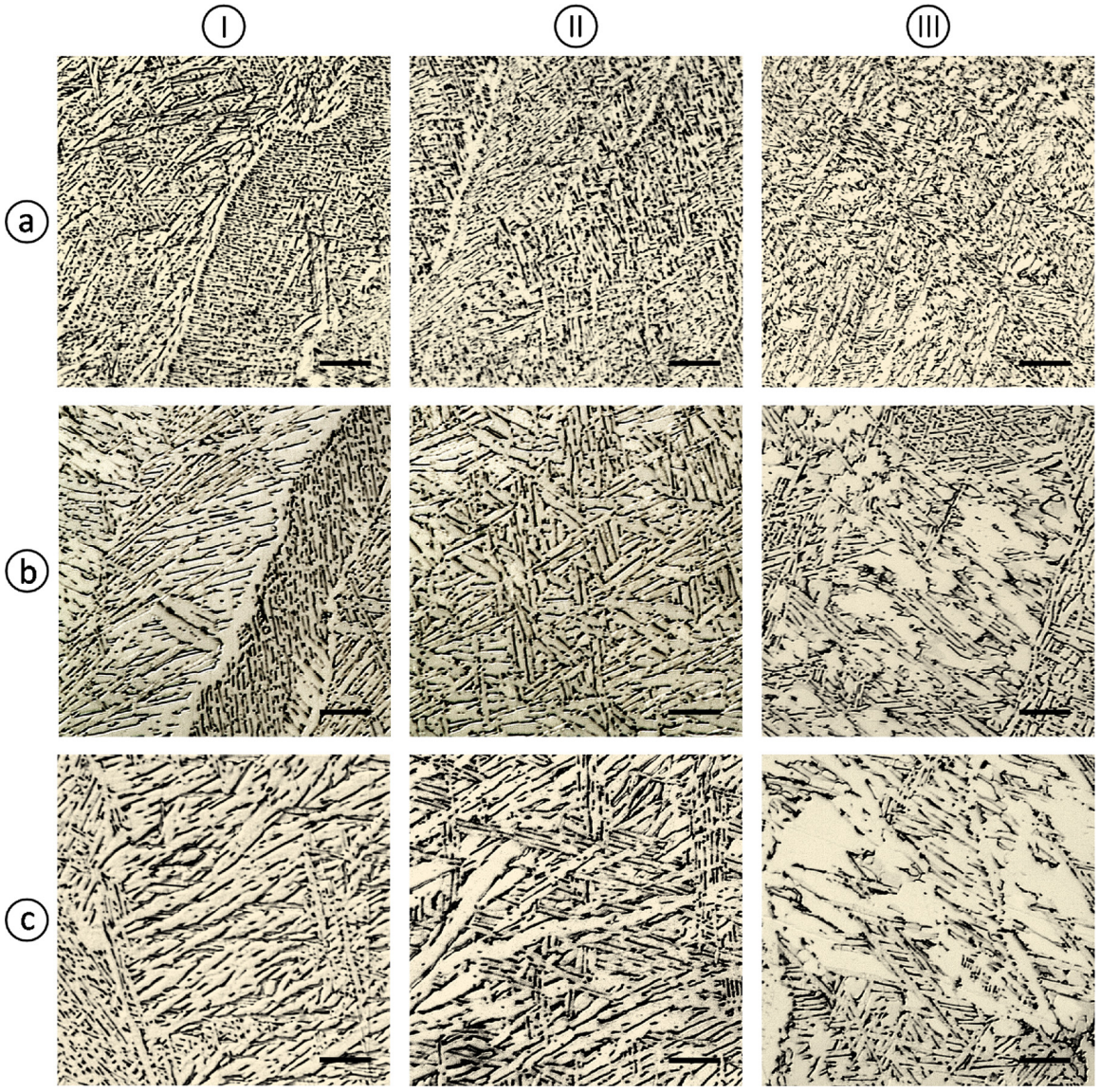

Fig. 4. Comparative illustration of (I) lamellar, (II) basketweave, and (III) large alfa grains in the specimens with (a) 1 mm thickness, (b) 3 mm thickness, and (c) 5 mm thickness. (Scale bar = 10 μm).

observable pattern of microstructures (basketweave and lamella). The quasi-stable crack growth stage followed the first stage of crack growth. This stage of crack growth consists of stable fatigue striations together with secondary cracks perpendicular to the crack growth plane (see Fig. 12c). The traces of microstructures in this stage of crack growth was less significant than the first stage. As the fatigue crack continued to propagate along the section, the stability of the crack growth deteriorated until it resulted in the final unstable crack growth. The unstable crack growth was identified by very tortuous surfaces having a combination of large fatigue striations and static failures (Fig. 12d). The tortuous features on the fracture surface were thought to follow the prior β grains in the material resulting in prior β intergranular failure and secondary cracks. Further propagation of the crack led to a ductile rupture of the material in a shear form indicated by ductile dimples on the fracture surface (Fig. 12e).

Comparative SEM fractographs of the tested specimens are shown in Figs. 13 and 14. Due to relatively high surface roughness of EBM specimens, fatigue cracks were initiated in all the specimens from the surface roughness (i.e., micro-notches on the surface). The fracture surface in all cases indicates three distinct areas of fatigue crack growth and ductile failure, which are separated in the figures using red lines and white dashed lines. Regardless of the thickness of the specimens, the fatigue crack initiation in unnotched specimens was mainly from one side of the net section propagating to the other side. Dealing with notched specimens, in some cases, the fatigue crack initiation occurred from both notches. In the case of specimens with 1 mm build thickness, although the main fatigue crack was started from the side face, continuous secondary fatigue crack initiation from the front and back faces of the specimens could be observed. This phenomenon is intensified due to higher surface roughness and roughness to thickness ratio in these specimens. According to Fig. 13, observable differences in the fatigue crack growth stages can be pointed out. While all the mentioned specimens were loaded under a maximum nominal applied load of ~ 200 MPa, the stability of fatigue crack propagation tends to decrease by decreasing the build thickness. Comparing the relative size of the stable crack growth stage to the whole fracture surface, both unnotched and notched specimens with 5 mm build thickness showed a broader stable crack growth region compared to the thinner specimens. Similar fatigue failure observations were also reported for cylindrical Ti-6Al-4V specimens produced with different diameters ranging from 3.25 to 6 mm [34].

As reported by Baragetti [49–52], larger stress gradient in the

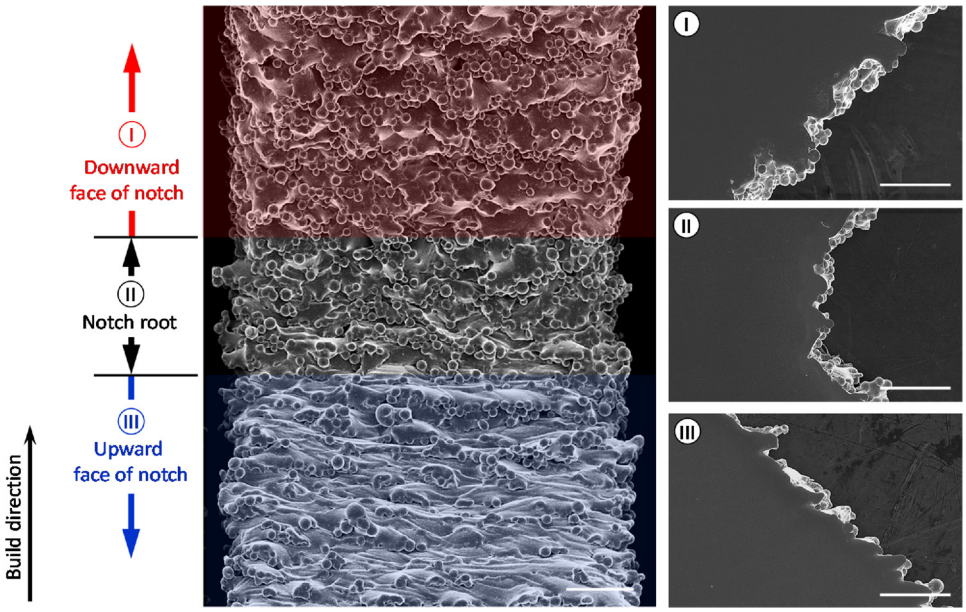

Fig. 5. SEM representation of (I) downward, (II) notch root, and (III) upward faces of the notch in the EBM specimen with 3 mm thickness. The pictures were taken from the side view of the notched specimen (i.e., YZ plane) showing the as-built surface condition and from the front view of the mid-thickness cut of the specimen (i.e., XZ plane). (Scale bar: 500 μm).

notched specimens results in early crack nucleation compared to their unnotched counterpart. They reported that although the steep stress variation along the width of the specimens results in fatigue crack initiation of notched components under lower stress levels, however, due to lower driving force of the fatigue crack in these geometries, the fatigue crack growth life is expected to be longer than the unnotched

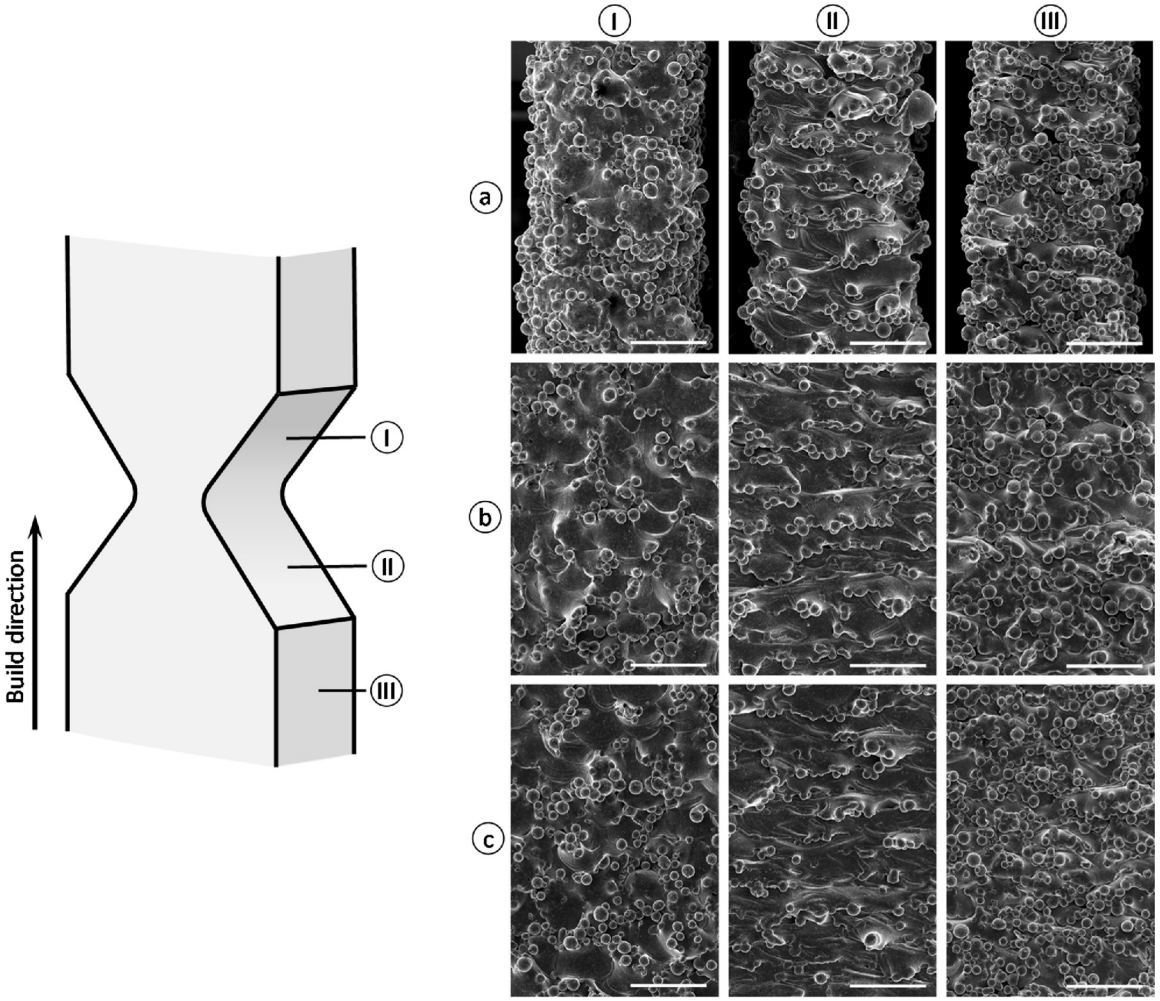

Fig. 6. Comparative SEM representation of (I) downward, (II) upward, and (III) side (i.e., parallel to the build direction) faces of notched region in the EBM specimen with (a) 1 mm, (b) 3 mm, and (c) 5 mm build thickness. The pictures were taken perpendicular to the surface. (Scale bar: 500 μm).

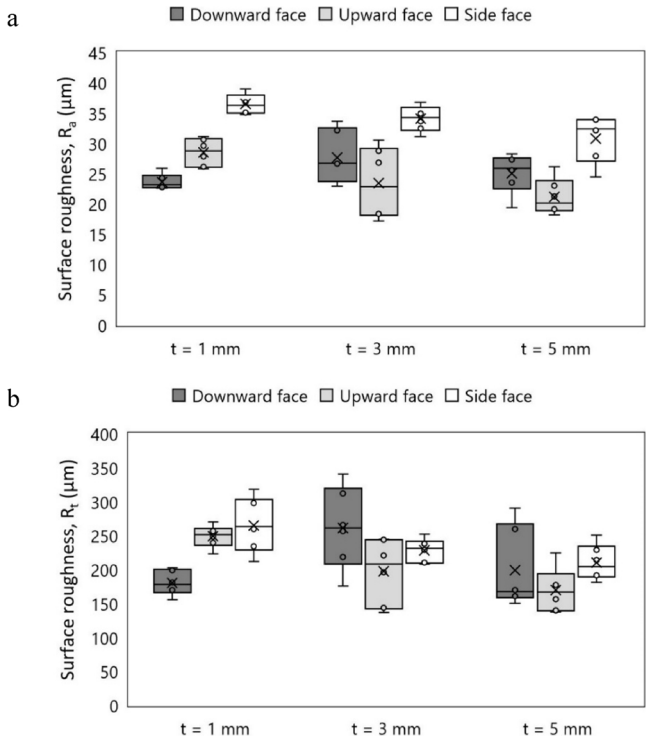

Fig. 7. Surface roughness of notched EBM specimens; (a) the arithmetic average of the roughness profile, R_a, (b) the maximum peak to valley height of roughness profile, R_t.

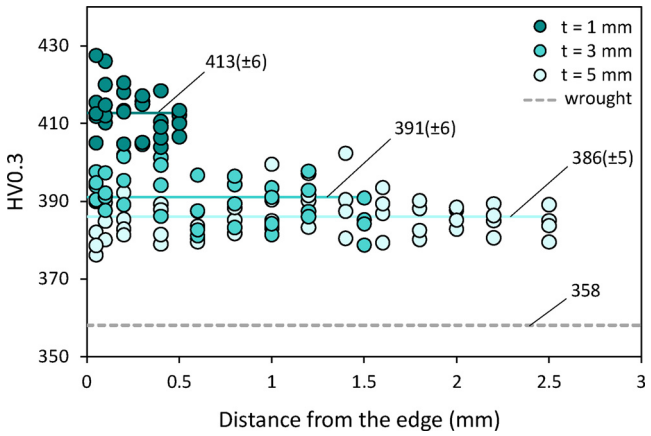

Fig. 8. Microhardness data of EBM specimens compared with wrought material.

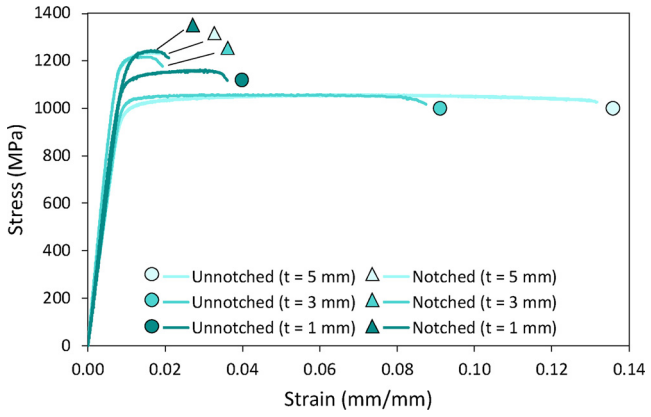

Fig. 9. Representative monotonic engineering stress-strain curves for the studied geometries.

geometry. This is somehow consistent with relatively larger size of the fatigue crack growth zone in the tested notched specimens.

Further investigations of fracture surface in higher magnifications revealed that the fatigue crack initiated from the root of micro-notches on the surface of the specimens (see Fig. 14). The presence of these micro-notches was due to the waviness of the surface due to the layered structure of the specimens. The morphology and texture of the fracture surface at fatigue crack initiation location was found to be somehow different in specimens with various build thicknesses. Since the fatigue failure is dependent on the microstructure of the material, it can be seen from Fig. 14 that the specimens with 1 mm thickness have finer texture compared to the thicker specimens. Additionally, although similar relatively coarse fracture micro-morphologies were observed in specimens with 3 mm and 5 mm thickness, however, presence of large flaky features due to transgranular failure of the grains in specimens with 5 mm thickness was evident. The fatigue crack initiation was then followed by propagation through the net section where the crack passes through the columnar prior β grains, including lamellar and basket-weave α + β structure. The presence of this complex microstructure was more evident in the thicker specimens. In these specimens, larger alfa grains leave a larger and more clear pattern on the fracture surface. According to Fig. 14(III), a clear mark is illustrated showing the boundary of prior beta grain within the material in the stable fatigue crack growth region. The fatigue crack growth continues until the final failure of the specimens with sudden rupture. The void coalescence ahead of the crack tip results in appearance of ductile dimples on the fracture surface of the ruptured area.

4. Discussion

Fatigue behavior of EBM Ti-6Al-4V specimens with different build thicknesses and in the presence of geometrical discontinuities has been evaluated in this study. The difference in appearance and mechanical behavior of the studied AM parts were correlated to the initial geometry of the part. Notch sensitivity analysis was performed using the the experimental fatigue limits of different specimen geometries.

According to the microstructure of EBM samples (see Fig. 2), sequential layer deposition during EBM process results in an epitaxial grain growth through the height of the specimens leading to a columnar prior-beta grain structure. These columnar grains can grow through several sintered layers of powder. These prior beta grains form after cooling and later on by further cooling turn to martensitic phases. Due to cyclic heating of the layers by the top sintered layers and also

Table 1
Average surface roughness measurements for as-built EBM notched specimens. (unit: μm).

Build thickness (mm)	Downward face		Upward face		Side face	
	R_a (STDEV)	R_t (STDEV)	R_a (STDEV)	R_t (STDEV)	R_a (STDEV)	R_t (STDEV)
1	23.08 (1.26)	180.60 (18.12)	28.53 (2.30)	248.93 (16.13)	36.50 (1.60)	264.97 (39.33)
3	27.67 (4.35)	261.60 (60.11)	23.42 (5.91)	197.51 (48.05)	34.09 (2.11)	228.61 (17.06)
5	25.03 (3.22)	199.39 (59.79)	21.13 (3.03)	169.73 (32.67)	30.82 (3.81)	210.26 (26.25)

Table 2
Average tensile properties of the tested specimens.

	Unnotched specimen			Notched specimen		
	t =5 mm	t =3 mm	t =1 mm	t =5 mm	t =3 mm	t =1 mm
Tensile strength (MPa)	1046	1065	1161	1224	1219	1239
Elongation at failure (%)	12.9	8.9	3.5	1.8	1.9	2.2

because of the heat-induced by the powder bed during the EBM process, the martensitic phases transform to the alfa phase within the prior beta grains. This consequently results in the development of a basketweave structure within the prior beta grains and alfa colonies close to the prior beta grain boundaries (see Fig. 3). This unique microstructure with fine α + β grains results in comparable ductility of EBM parts compared to wrought counterpart [53].

According to Fig. 4, a clear trend between the microstructure of specimens with different thicknesses can be observed. Thicker specimens have higher mass (m), which is capable of storing more heat, mc_p (c_p: specific heat capacity of the material at constant pressure). As a result, these parts with longer scan time experience slower cooling rate and consequently longer term annealing at a higher temperature in comparison with the thinner parts. The slower cooling rate in thicker part facilitates the grain growth. This grain growth was observed in both basketweave microstructure (within the prior beta grains) and lamellar microstructure (next to the boundaries of prior beta grains). In the case of specimens of 3 mm and 5 mm thickness, a limited number of large globular alfa grains were observed within the basketweave microstructure. These findings are in line with the numerical analysis of temperature profiles in specimens of different build thickness reported by Tan et al. [23]. They reported a faster kinetics for martensite decomposition for thicker samples due to higher average temperature in this samples compared to the thinner counterparts.

These distinct microstructures in EBM parts of various build thickness consequently resulted in different microhardness values and tensile properties of the material. Due to finer grains in the studied EBM specimens compared to the wrought material [37], higher microhardness values were obtained. A comparative observation reveals that the 1 mm thick specimen with the finest microstructure had a higher microhardness value, which was around 7% higher than that of the 5 mm thick specimen and about 15 % higher than the wrought material.

The tensile tests revealed a slightly higher tensile strength of 1 mm thick specimens, which can be correlated to the finer grains resulted from higher cooling rate during the manufacturing. Unlike the tensile strength, elongation at failure of the parts of different thicknesses was strongly dependent on the build thickness having the highest value for the largest thickness. This can be attributed to the larger grain size of bulk material in thicker specimens and smaller length ratio of the micro-notch to the thickness of the specimen. Considering the tensile behavior of notched specimens, inducing notches in thicker specimens with higher stress triaxiality levels resulted in stronger notch strengthening effect and consequently higher increase of load-bearing capacity and reduction in elongation at failure.

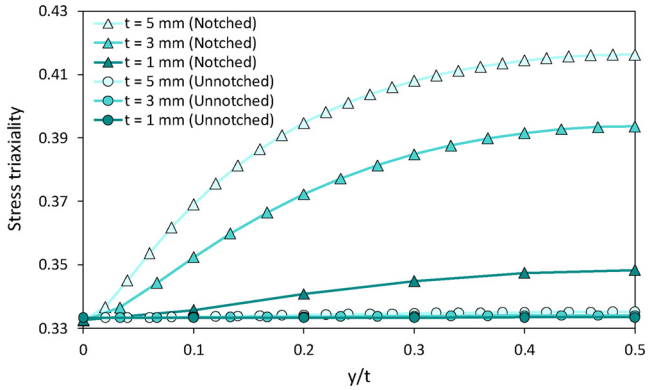

Fig. 10. The variation of stress triaxiality along the thickness of different test specimens. y is the distance along the thickness, while t is the build thickness (y/t = 0.5 represents the mid-thickness of the parts).

The EBM specimens with different build thickness experience different thermal histories and production accuracies during the manufacturing which consequently can result in unsimilar microstructure and surface morphology. One important point about the specimens with lower thicknesses is fewer number of scan tracks in these components resulting in lack of laser energy input, which may lead to insufficient melting, creation of irregular morphologies and open defects on the surface (see Fig. 6) and pore formation within the component. This can

Table 3
Comparative tensile properties of EBM specimen with the data available in literature.

	Build thickness (mm)	Tensile strength (MPa)	Elongation at failure (%)	Description
Current study	5	1046	12.9	As-built
	3	1065	8.9	As-built
	1	1161	3.5	As-built
Wysocki et al. [38]	15	972	14.2	As-built machined
Zhai et al. [39]	≈ D10	1073 - 1116	11.0 – 15.0	As-built machined
Zhao et al. [40]	D7	1035	13.8	As-built
Zhao et al. [40]	D4	1044	14.5	As-built
Chastand et al. [41]	D4	1045	10.9	As-built machined
de Formanoir et al. [42]	2	≈ 850	3.6	As-built
Dzugan et al. [43]	2.52	806	3.9	As-built
Zhao et al. [40]	D1.2	1176	2.2	As-built
Dzugan et al. [43]	0.62	480.5	2.3	As-built
Arcam [44]	–	1020	14.0	As-built
Wrought [38,45,46,47,48]	–	933 - 1063	12.5 - 14	
Forged [2,48]	–	1006 - 1030	16.0 - 18.4	Mill anealed
Cast [47]	–	875	4.5	
ASTM F1108	–	860	> 8	For cast material
ASTM F1472	–	930	> 10	For wrought material
ASTM F136	–	> 860	> 10	For wrought material used in surgical implant applications

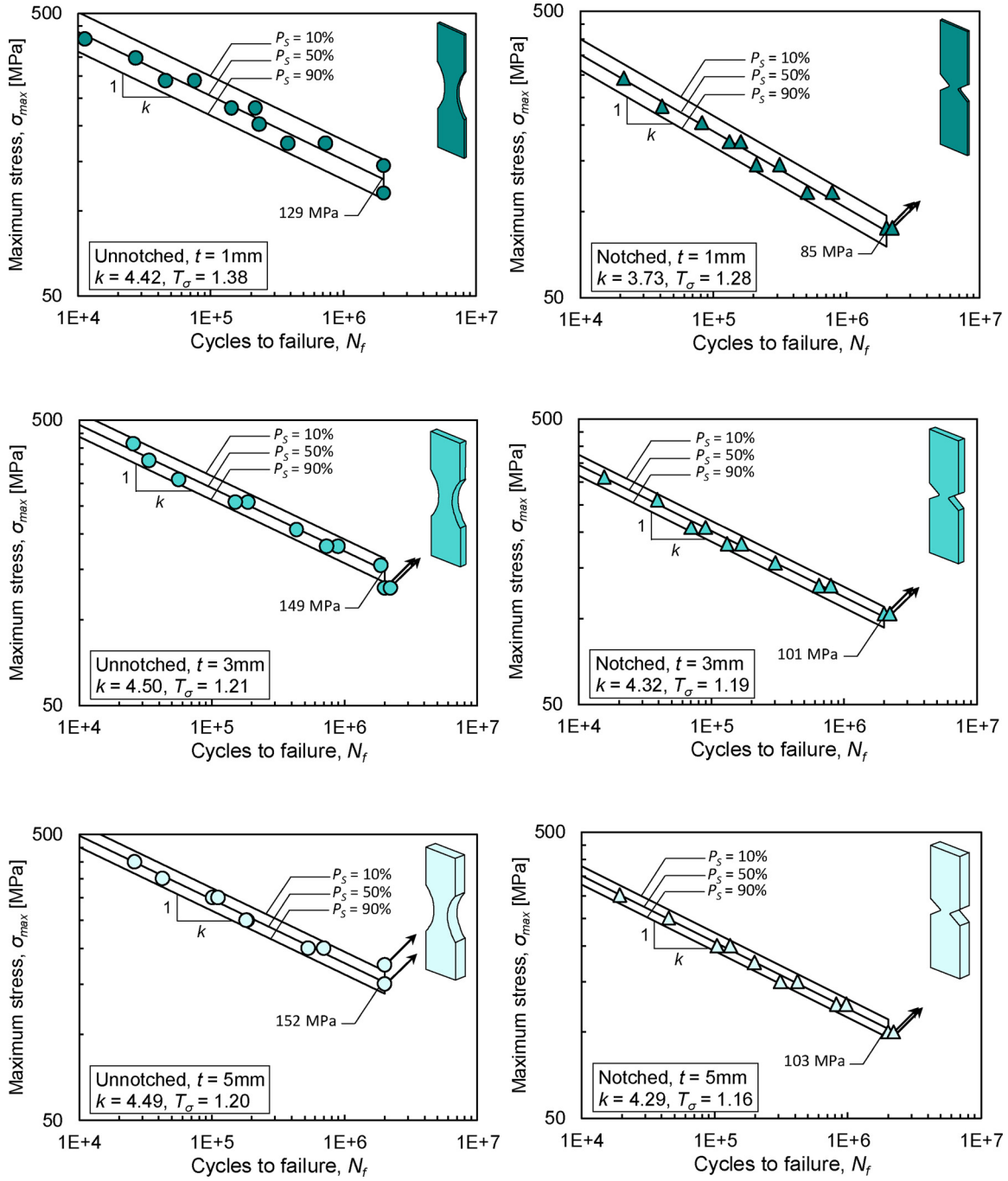

Fig. 11. Fatigue data from different specimen geometries made by EBM process tested under loading ratio of $R = 0$ and 30 Hz loading frequency.

Table 4
Fatigue behavior of tested Ti-6Al-4V specimens.

Geometry	Thickness [mm]	$\Delta\sigma_{50\%}$[a] [MPa]	T_σ	k	K_t	K_f	q
Unnotched	1	129	1.38	4.42	1.07	–	–
	3	149	1.21	4.50	1.08	–	–
	5	152	1.20	4.49	1.08	–	–
Notched	1	85	1.28	3.73	2.34	1.52	0.39
	3	101	1.19	4.32	2.41	1.48	0.34
	5	103	1.16	4.29	2.43	1.48	0.33

[a] Fatigue strength at 2×10^6 cycles.

consequently increase the surface roughness of the specimens with lower build thickness. The higher surface roughness results in higher intensified stresses on the surface of the part leading to lower fatigue crack initiation life. On the other hand, the specimens with the highest build thickness were found to have the lowest surface roughness making them more resistant to fatigue crack initiation compared to the case of the same material with higher surface roughness. Additionally, materials with larger grains have a higher resistance to fatigue crack propagation. According to Fig. 13, it was observed that the specimens with larger build thickness and grain size experienced longer stable crack growth. A combination of these two points for the thicker parts with lower surface to volume ratio and larger grain size resulted in higher overall fatigue lives of these specimens compared to the thinner counterparts. It should be noted that the surface to volume ratio is as an

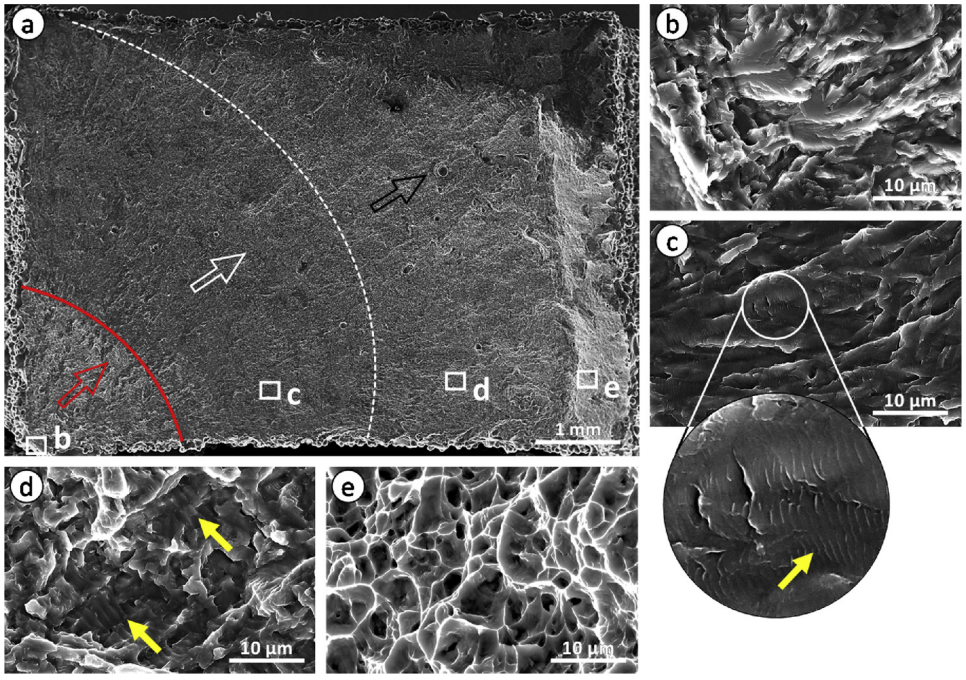

Fig. 12. Representative fatigue crack growth stages on the fracture surface of tested specimens.

important factor influencing the fatigue behavior [34,54,55]. In this case, for a constant surface roughness value, reducing the build thickness increases the surface to volume ratio, increasing the fatigue initiation sites and consequently reduces the fatigue life of the component.

The fatigue crack initiation in Ti-6Al-4V alloy with alpha Hexagonal Close Packed (HCP) and beta Body Central Cubic (BCC) crystal lattice characteristics, occurs within the alfa grains. Hence the morphology and size of the alfa phase in the material can directly affect the fatigue properties [56,57]. Considering the lattice structure of the HCP alfa phase, only a limited number of slip systems occur within this phase, which are all parallel to each other (planes (0001) in the Miller-Bravais system). This limited number of slip systems compared to Cubic Crystal (CC) structures lowers the likelihood of moving mobile dislocations in favorable planes resulting in a lower probability of formation of intrusions and extrusions, which are the prominent origin of fatigue crack initiation in the material [57]. Considering a notch geometry in the test specimen, a fewer number of potential crack initiation sites exist in the reduced area of a notched specimen compared to the unnotched geometry. The number of these potential crack initiation sites in the notch

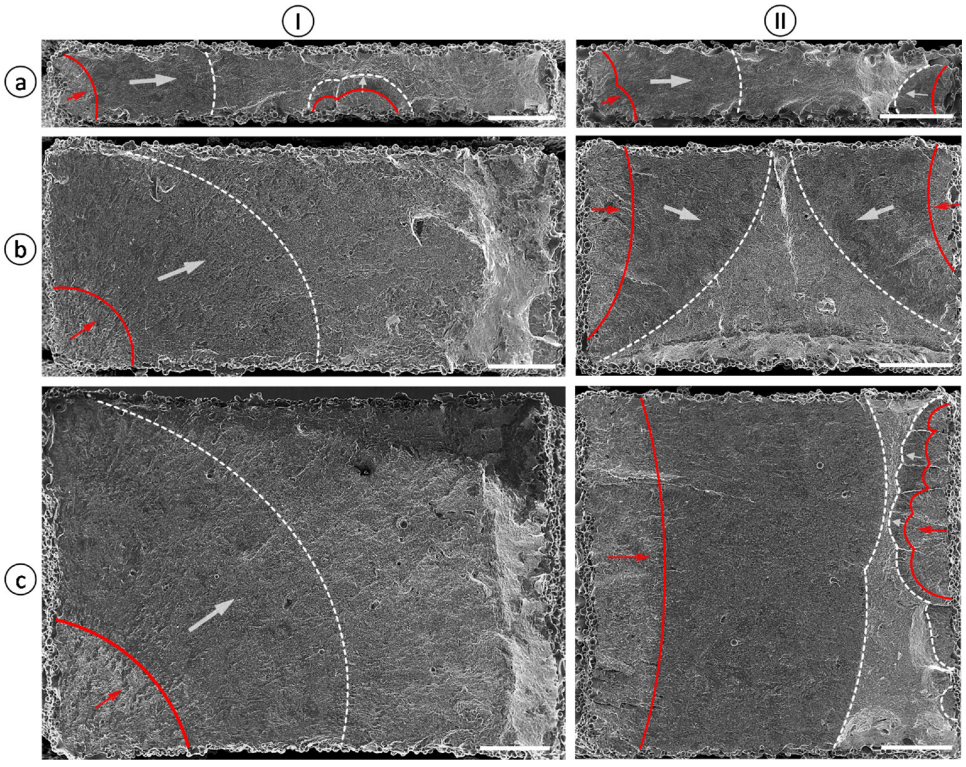

Fig. 13. SEM fractographs of the fatigue fracture surface obtained from the tested EBM specimens of build thickness (a) 1 mm, (b) 3 mm, (c) 5 mm under maximum stress of 200 MPa. (I) Unnotched and (II) notched geometries. Red arrows indicate the first stage of crack growth (i.e., stable crack growth), resulting in lighter surface color due to the tortuous morphology. White arrows indicate the quasi-stable crack growth with darker surface color separated by white dashed lines from the unstable crack growth and ductile failure stage. (Scale bar =1 mm).

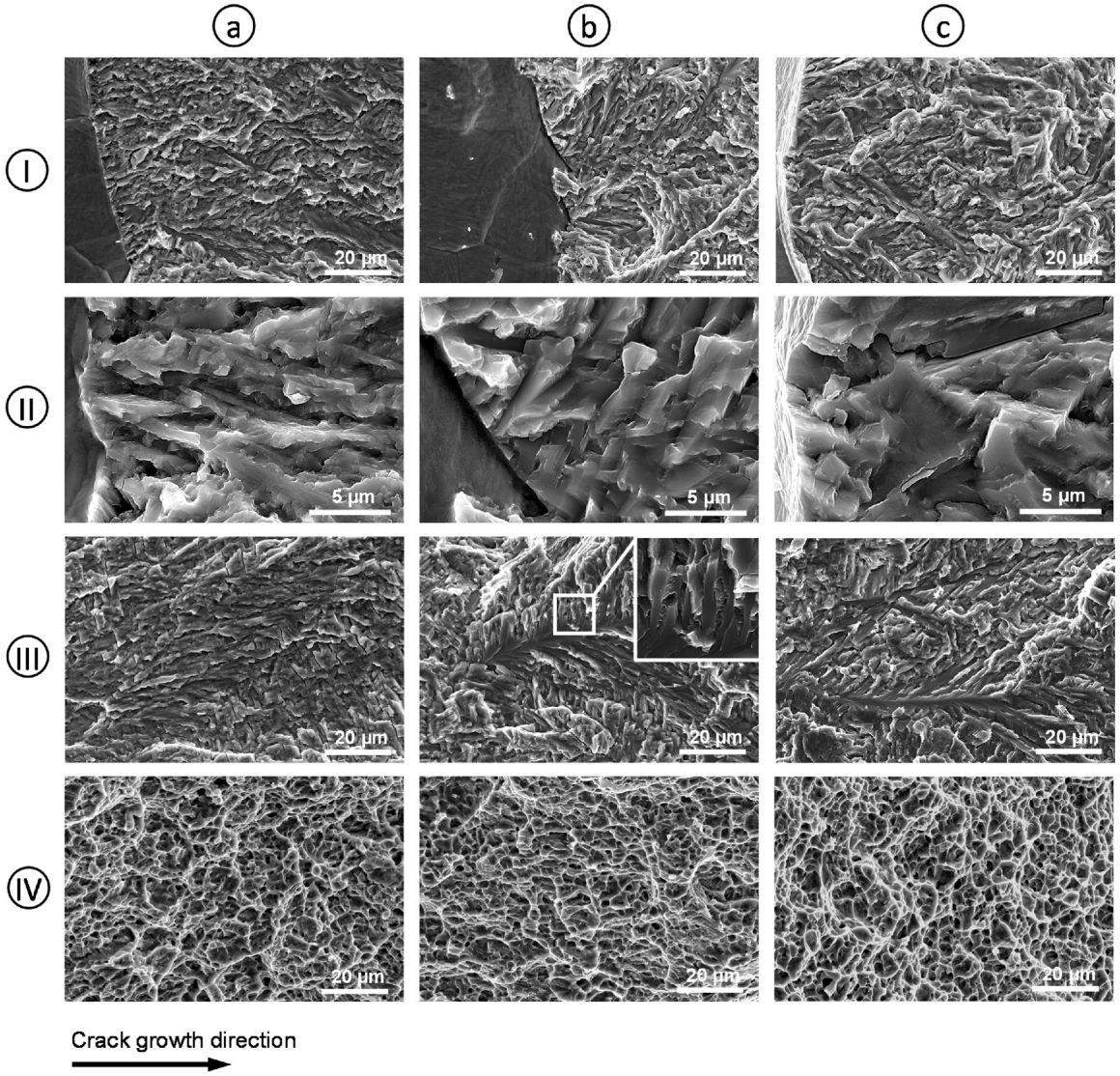

Fig. 14. SEM fractographs of the tested EBM specimens with (a) 1 mm, (b) 3 mm, and (c) 5 mm build thickness. (I, II) fatigue crack initiation from the edge, (III) fatigue crack propagation through the section, (IV) ductile failure surface. Traces of crack propagation through the prior beta grains are shown in b(III) and c(III) (the black arrow shows the direction of fatigue crack propagation).

region can increase for the material with finer microstructure making that material more sensitive to the presence of the notch and consequently resulting in higher notch sensitivity of the material.

In another scenario, higher roughness and presence of surface defects reduced the fatigue resistance of both unnotched and notched specimens having the opposite effect compared to the effect of grain size on the notch sensitivity. Overall, although higher notch sensitivity is expected for the thinner specimens with finer grains, however, only slightly higher notch sensitivity of 0.39 (t = 1 mm) compared to 0.34 (t = 3 mm) and 0.33 (t = 5 mm) was due to opposing effect of higher surface to volume ratio in thin specimens. It can be argued that the notch sensitivity values do not specifically describe the material behavior but rather a combination of material properties and the geometry of the parts. In this scenario, varying only one parameter (e.g. thickness or microstructure) would result in better understanding of the sources of variation in fatigue properties. This task requires further studies where thermal post-treatment or surface machining be used to evaluate the sole influence of surface roughness and microstructures on the notch sensitivity of the EBM components.

Generally, two categories of global discontinuities (notch geometries) and local discontinuities (i.e., defects and surface roughness) are available in AM materials. For the notched specimens with high stress concentration factor, it is assumed that the global discontinuities govern the failure. While for the specimens with low stress concentration factor, the local discontinuities can govern fatigue failure. The stress concentration factor, the surface condition, and the number of defects are the critical parameters in defining the governing failure mechanisms. Considering the micro-notches on the surface of specimens as crack initiation sites, there are a lower number of micro-notches in the notch root area of the specimens compared to the larger length of the reduced area in the unnotched specimens. In this case, due to lack of a global stress concentrator (i.e., V notch) in the unnotched specimens, the fatigue crack can initiate in a range of specimen's height. According to the curved shape of the reduced area in unnotched specimens, if the fatigue crack initiated in different points along the height of the specimens for different cases, a higher scatter of the fatigue results would be obtained mainly due to variation in the section area which varies along the height of the specimen. This larger scatter of fatigue data for unnotched specimens can be seen in Fig. 11, regardless of the build thickness. As mentioned earlier, lower surface roughness values were obtained for EBM specimens with 5 mm thickness, and the surface morphology, in this case, was more consistent between

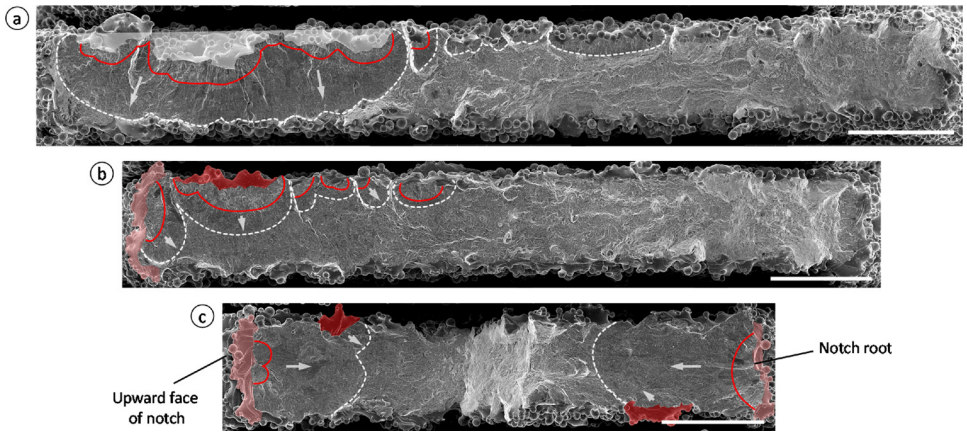

Fig. 15. SEM fractographs of the tested EBM specimens with 1 mm build thickness. (a) Failure from a deep inclusion on the front face of the unnotched specimen. Failure, in this case, has not happened in the mid-height of the specimen resulting in a larger fracture surface. (b) Failure from the side and the front face of an unnotched specimen. The deepest micro-notches on the side (in pink) and front (in red) faces were the initiation locations. (c) Failure from both sides in a notched specimen. Fatigue failure started from the lower region of the notch (upward face) on one side and notch root on the other side. The final fracture follows a shear plane connecting these two crack planes.

specimens of this build thickness. This consistency of the surface condition consequently resulted in smaller scatter bands of fatigue data in these specimens compared to the specimens with the lowest build thickness. Complex fatigue crack initiation and propagation mechanisms with multiple crack initiation sites were observed in the specimens with 1 mm build thickness tested under fatigue loading. Fig. 15 illustrates the fracture surface of some EBM specimens with 1 mm thickness. As a clear source of higher scatter in this set of specimens, two main reasons can be pointed out. First, the presence of irregular surface defects in some of the specimens (see Fig. 15), resulting in lower fatigue life and failure from a plane other than the mid-plane of the specimen. Second, multiple crack initiation from several faces (side and front) and the interaction of these cracks results in a more complex failure in the part, making the fatigue life dependent on the configuration of the micro-notches, which are the sources of crack initiation in the specimens. In all cases, the largest micro-notches were the competing location for the fatigue crack to start from. The presence of deep micro-notches on the front face of some of the specimens with 1 mm thickness was thought to be the reason for fatigue crack initiation from this location.

Dealing with fatigue failure location in the EBM parts, one can consider surface roughness as a key parameter. The notched specimens with the overhang surface showed anisotropic surface roughness, having large micro-notches on the downward face (see Fig. 5) and smaller but sharper micro-notches on the upward face of the specimen. The fatigue crack tends to start from the micro-notch with the highest notch acuity. Depending on the geometry of the micro-notches on the downward, notch root, and upward faces, different failure locations along the height of the notch specimens were observed in the specimen, with the majority of them starting from the notch root. No clear dependency of the fatigue crack initiation on the build thickness was observed in the tested specimens.

According to the fractography results, in all tested specimens with different geometries, the fatigue crack was starting from surface roughness following a microstructure dependent phase of crack growth (stable crack growth), quasi-stable crack growth, unstable crack growth, and final ductile rupture. Overall, the fatigue crack interaction with columnar beta grain boundaries contributed to the patterned morphologies on the fracture surface, leading to more roughness induced closure effects during fatigue crack propagation. A similar observation was reported previously indicating a typical acceleration and retardation in fatigue crack growth rate of AM materials [56].

Fig. 16 illustrates a comparative representation of fatigue behavior of Ti-6Al-4V produced by EBM and conventional methods. The fatigue data in this figure are presented as effective stress, σ_{eff} versus number cycles. The concept of effective stress was first introduced by Li et al. [58] and it was used to directly compare fatigue data from different sources. Different fatigue studies usually use a wide range of stress

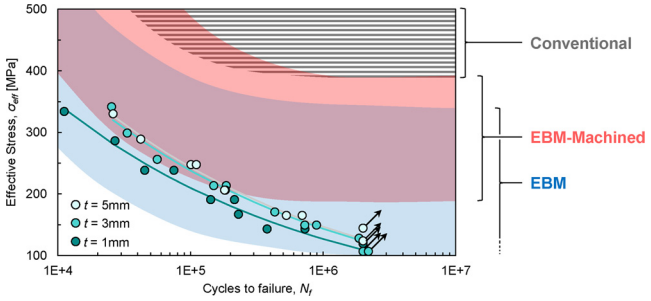

Fig. 16. Comparative fatigue behavior of unnotched EBM specimens (tendencies extracted from [62]).

ratios, R for fatigue testing. According to the effective stress model, fatigue data under various stress ratios can be normalized into a single fatigue plot using the following equation:

$$\sigma_{eff} = \sigma_{\max}\left(\frac{1-R}{2}\right)^{0.28} \quad (1)$$

This model, however, does not consider the effect of loading frequency. Frequency effects are normally sensible over orders of magnitude difference in frequency [59–61]. Nevertheless, since the majority of available fatigue data in literature are within a frequency range of 20 − 120 Hz, limited effect of loading frequency is expected [62].

According to Fig. 16, the fatigue data of current research lies within the data range from previous studies. As expected, EBM parts with as-built surface condition show considerably lower fatigue strength compared to the parts produced by conventional techniques. This significant fatigue strength reduction (up to 75 %) is mainly due to high surface roughness value of EBM parts being in a range of R_a = 25 − 131 µm [63,64]. Regardless of geometry and dimensions of AM parts, process parameters play a major role in surface roughness of produced components. Process conditions for reduction of surface roughness include reduced layer thickness and powder size [65–67] and application of optimized contour scanning [68].

Although the high surface roughness of EBM parts is preferred for osseointegration in biomedical applications [67], presence of sharp micro-notches on the surface is detrimental in case of cyclic loading. Various techniques such as surface machining [41], laser ablation [67], rotary ultrasonic machining [69], chemical etching [70] have been proposed in the literature to improve the fatigue performance of EBM parts. Each of these techniques can potentially improve the fatigue strength to a level comparable to the wrought counterpart [71]. However, their application can be limited by cost, geometric considerations, increased build time, and post-processing [62]. As shown in Fig. 16, surface machining improves the fatigue behavior, however, the fatigue performance of machined parts are still far from the reported values for

conventional material. This is mainly due to residual sharp notches and defects on the surface of the machined AM parts [62,72,73]. Hot Isostatic Pressing (HIP) on the other side, is a post-processing technique that is recommended for reducing the internal porosity of EBM components. This technique significantly improves fatigue strength of EBM parts which have been surface machined [74–76]. The dependency of efficiency of the mentioned post-processing techniques is believed to be dependent on the geometry and size of EBM parts. Hence, further studies should be conducted to accurately investigate this matter.

According to the experimental observations reported in this research, the appearance and consequently mechanical behavior of EBM specimens under quasi-static and fatigue loading conditions is dependent on the thickness and geometry of the required part. Although a trend of variation in different material properties was observed, however, predicting the microstructural characteristics and the geometrical accuracy of EBM parts and the level of their dependence on the scale, geometry and process parameters is still to be studied.

5. Summary and conclusions

The current research aimed to evaluate the build thickness effect and effect of the presence of geometrical discontinuities on the mechanical properties of EBM Ti-6Al-4V under quasi-static and fatigue loading conditions. Based on the experimental results analyses presented, the following conclusions can be drawn:

1) The grain size in EBM specimens was observed to be dependent on the build thickness having the larger value in the specimens with the highest thickness. This was attributed to the lower cooling rate in the thicker specimens of 5 and 3 mm which allows continuous growth of the grains resulting in considerably larger grain size of 1.9 and 1.3 μm compared to fine microstructures of 0.7 μm observed for the specimens of 1 mm thickness.
2) The lower build thickness of EBM parts resulted in higher surface roughness, which can be due to a smaller number of tracks on the section of the parts resulting in insufficient melting, creation of irregular morphologies and open defects on the surface and pore formation within the component.
3) The experimental results show that elongation at failure significantly increased by ~ 270% with the increase in build thickness. The higher ductility of the thicker parts of 5 mm thickness was attributed to the larger grain size, resulting also in ~ 7% lower microhardness compare to the specimens with 1 mm build thickness. The numerical results revealed ~ 20% larger stress triaxiality in 5 mm thick notched specimens compared to the ones with 1 mm build thickness. This higher ductility together with higher stress triaxiality intensified the notch strengthening effect and leads to an increase of ~ 150% and ~ 130% in tensile strength enhancement and reduction of elongation at failure with increase in the build thickness.
4) The effect of surface roughness on high cycle fatigue behavior of specimens with smaller thickness was found to be more significant. Lower fatigue strength of thinner specimens was ascribed to the higher surface to volume ratio, higher surface roughness and randomly distributed deep micro-notches on the surface. The very rough surface of thinner specimens composes a larger portion of total cross section (due to high ratio of micro-notche depth to thickness). This effect together with the higher strength of thin specimens intensifies the effect of surface roughness on fatigue resistance and results in lower fatigue lives in this specimens.
5) In the case of notched specimens, two aspects can lead to the notch sensitivity of the materials; micromechanical aspect and geometry aspect (i.e., surface roughness). From the micromechanical aspect, thinner specimens with finer grains experience higher occurrence possibility of persistent slip bands in the small volume in the vicinity of the notch tip resulting in higher notch sensitivity compared to the thicker parts with coarser microstructure. On the other side, the presence of micro-notches on the surface of both unnotched and notched specimens reduces the fatigue notch factor and consequently results in lower notch sensitivity. Considering the studied cases, slightly higher notch sensitivity was observed in the specimens of 1 mm thickness, revealing the surface roughness as the dominant factor in notch fatigue behavior of these specimens.

Funding

None.

Data availability

The presented data in this research will be made available upon request.

CRediT authorship contribution statement

S.M.J. Razavi: Conceptualization, Methodology, Investigation, Data curation, Visualization, Writing - original draft. **B. Van Hooreweder:** Writing - review & editing. **F. Berto:** Conceptualization, Methodology, Writing - review & editing.

Declaration of Competing Interest

The authors declared no conflicts of interest.

Appendix A

Three-dimensional finite element analyses were performed on the models with different geometries using ABAQUS 2017 software. The elastic modulus of $E = 110$ GPa and the Poisson's ratio of $\nu = 0.34$ were considered for finite element modeling. Due to the symmetry of the test specimens, only one-eighth of the geometry was modeled by considering triple symmetric boundary conditions along the width, length, and thickness of the model. Unit negative pressure was applied to the gross section of the models to evaluate the stress variation and stress triaxiality. The 20-node quadratic brick elements (C3D20R) were used for three-dimensional stress analysis. As illustrated in Fig. A1, higher mesh density was used near the notch root to improve the accuracy of the results. A mesh convergence study was also undertaken to ensure that a proper element size was used for model discretization by considering the von Mises stress as the key parameter in the convergence analysis. Getting away from the notch region with an element size of 100 μm, the element size was coarsened to 2 mm.

Due to the comparative aim of the finite element analysis, the material heterogeneity and the effect of surface roughness were neglected in the analysis to provide only a qualitative explanation of build thickness effect on the stress state at the notch root. As the outcome of the analyses, three principal stresses together with von Mises stress were extracted from the notch root along the thickness of the model. These stress values were then substituted in the following equation to calculate the stress triaxiality level:

$$\beta_t = \frac{\sigma_m}{\sigma_{eq}} \tag{A.1}$$

where

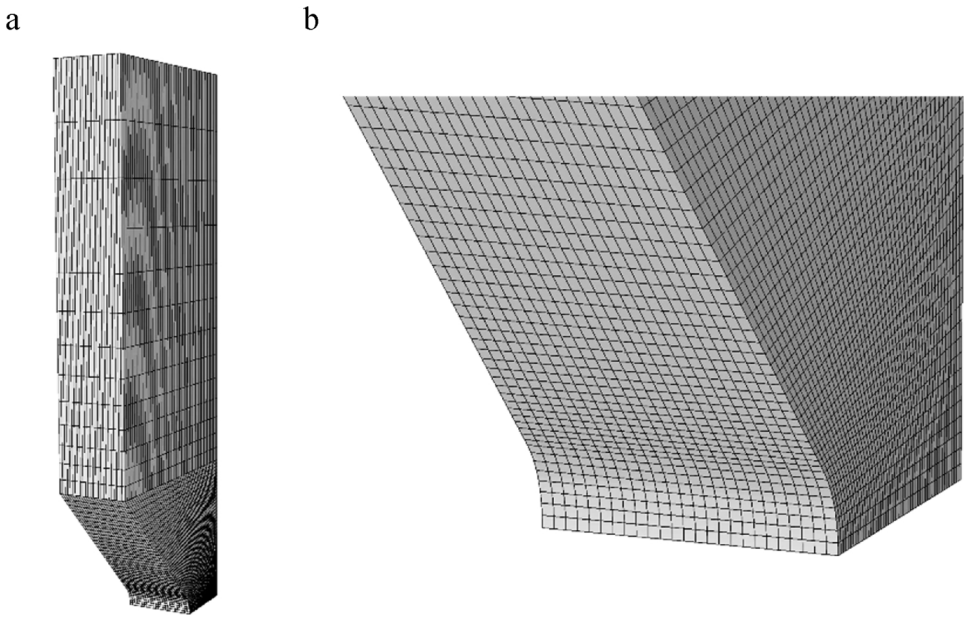

Fig. A1. Representative mesh pattern in notched model with 5 mm thickness.

$$\sigma_m = \frac{1}{3}(\sigma_1 + \sigma_2 + \sigma_3) = \frac{1}{3}(\sigma_x + \sigma_y + \sigma_z) \tag{A.2}$$

in which, β_t is stress triaxiality, σ_m is the mean stress, σ_{eq} is the equivalent von Mises stress, σ_i (i = 1,2,3) are the principal stresses, and σ_i (i = x,y,z) are the stress components in different directions.

Appendix B. Supplementary data

Supplementary material related to this article can be found, in the online version, at doi:https://doi.org/10.1016/j.addma.2020.101426.

References

[1] Frazier WE, Metal additive manufacturing: a review, J. Mater. Eng. Perform. 23 (6) (2014) 1917–1928.

[2] C. Selcuk, Laser metal deposition for powder metallurgy parts, Powder Metall. 54 (2011) 94–99.

[3] F. Berto, S.M.J. Razavi, J. Torgersen, Frontiers of fracture and fatigue: some recent applications of the local strain energy density, Frat Ed Integrita Strutt 12 (2018) 1–32.

[4] L.E. Lindgren, A. Lundback, M. Fisk, R. Pederson, J. Andersson, Simulation of additive manufacturing using coupled constitutive and microstructure models, Addit. Manuf. 12 B (2016) 144–158.

[5] N.N. Kumbhar, A.V. Mulay, Post processing methods used to improve surface finish of products which are manufactured by additive manufacturing technologies: a review, J. Inst. Eng. Ser. C 99 (4) (2018) 481–487.

[6] Tangestani R., Farrahi G.H., Shishegar M., Pourbagher Aghchehkandi B., Ganguly S., Mehmanparast A., Effects of vertical and pinch rolling on residual stress distributions in wire and arc additively manufactured components, J. Mater. Eng. Perform. (in press) (https://doi.org/10.1007/s11665-020-04767-0).

[7] S. Bagherifard, N. Beretta, S. Monti, M. Riccio, M. Bandini, M. Guagliano, On the fatigue strength enhancement of additive manufactured AlSi10Mg parts by mechanical and thermal post-processing, Mater. Des. 145 (2018) 28–41.

[8] du Plessis A., Macdonal E., Hot isostatic pressing in metal additive manufacturing: X-ray tomography reveals details of pore closure, Addit. Manuf. (in press) (https://doi.org/10.1016/j.addma.2020.101191).

[9] A. du Plessis, D. Glaser, H. Moller, N. Mathe, L. Tshabalala, B. Mfusi, R. Mostert, Pore closure effect of laser shock peening of additively manufactured AlSi10Mg, 3D Print. Addit. Manuf. 6 (2019) 245–252.

[10] G. Tapia, A. Elwany, A review on process monitoring and control in metal-based additive manufacturing, J. Manuf. Sci. Eng. 136 (6) (2014) 060801.

[11] N. Shamsaei, A. Yadollahi, L. Bian, S.M. Thompson, An overview of direct laser deposition for additive manufacturing; Part II: mechanical behavior, process parameter optimization and control, Addit. Manuf. 8 (2015) 12–35.

[12] S. Raghavan, M.L.S. Nai, P. Wang, W.J. Sin, T. Li, J. Wei, Heat treatment of electron beam melted (EBM) Ti-6Al-4V: microstructure to mechanical property correlations, Rapid Prototyp. J. 24 (4) (2018) 774–783.

[13] L.E. Murr, E.V. Esquivel, S.A. Quinones, S.M. Gaytan, M.I. Lopez, E.Y. Martinez, F. Medina, D.H. Hernandez, E.Y. Martinez, J.L. Martinez, S.W. Stafford, D.K. Brown, T. Hoppe, W. Meyers, U. Lindhe, R.B. Wicker, Microstructures and mechanical properties of electron beam-rapid manufactured Ti-6Al-4V biomedical prototypes compared to wrought Ti-6Al-4V, Mater. Charact. 60 (2) (2009) 96–105.

[14] S. Rawal, J. Brantley, N. Karabudak, Additive manufacturing of Ti-6Al-4V alloy components for spacecraft applications, RAST 2013 - Proc.6th Int. Conf. Recent Adv. Sp. Technol. (2013), https://doi.org/10.1109/RAST.2013.6581260).

[15] M. Neikter, P. Åkerfeldt, R. Pederson, M.L. Antti, V. Sandell, Microstructural characterization and comparison of Ti-6Al-4V manufactured with different additive manufacturing processes, Mater. Charact. 143 (2018) 68–75.

[16] A. Safdar, L.Y. Wei, A. Snis, Z. Lai, Evaluation of microstructural development in electron beam melted Ti-6Al-4V, Mater. Charact. 65 (2012) 8–15.

[17] S.S. Al-Bermani, M.L. Blackmore, W. Zhang, I. Todd, The origin of microstructural diversity, texture, and mechanical properties in electron beam melted Ti-6Al-4V, Metall. Mater. Trans. A Phys. Metall. Mater. Sci. 41 (2010) 3422–3434.

[18] P. Wang, M.L.S. Nai, W.J. Sin, J. Wei, Effect of building height on microstructure and mechanical properties of big-sized Ti-6Al-4V plate fabricated by electron beam melting, MATEC Web Conf. 30 (2015) 2001.

[19] B. Vrancken, L. Thijs, J.P. Kruth, J. Van Humbeeck, Heat treatment of Ti6Al4V produced by selective laser melting: microstructure and mechanical properties, J. Alloys Compd. 541 (2012) 177–185.

[20] C. de Formanoir, S. Michotte, O. Rigo, L. Germain, S. Godet, Electron beam melted Ti-6Al-4V: microstructure, texture and mechanical behavior of the as-built and heat-treated material, Mater. Sci. Eng. A 652 (2016) 105–119.

[21] N. Hrabe, T. Quinn, Effects of processing on microstructure and mechanical properties of a titanium alloy (Ti-6Al-4V) fabricated using electron beam melting (EBM), part 1: distance from build plate and part size, Mater. Sci. Eng. A 573 (2013) 264–270.

[22] N. Hrabe, T. Quinn, Effects of processing on microstructure and mechanical properties of a titanium alloy (Ti-6Al-4V) fabricated using electron beam melting (EBM), Part 2: energy input, orientation, and location, Mater. Sci. Eng. A 573 (2013) 271–277.

[23] X. Tan, Y. Kok, Y.J. Tan, G. Vastola, Q.X. Pei, G. Zhang, Y.W. Zhang, S.B. Tor, K.F. Leong, C.K. Chua, An experimental and simulation study on build thickness dependent microstructure for electron beam melted Ti-6Al-4V, J. Alloys Compd. 646 (2015) 303–309.

[24] W. Toh, P. Wang, X. Tan, M. Nai, E. Liu, S. Tor, Microstructure and wear properties of electron beam melted Ti-6Al-4V parts: a comparison study against as-cast form, Metals 6 (2016) 284.

[25] X. Tan, Y. Kok, W.Q. Toh, Y.J. Tan, M. Descoins, D. Mangelinck, S.B. Tor, K.F. Leong, C.K. Chua, Revealing martensitic transformation and α/β interface evolution in electron beam melting three-dimensional-printed Ti-6Al-4V, Sci. Rep. 6

(2016) 1–10.
[26] Y.H. Kok, X.P. Tan, N.H. Loh, S.B. Tor, C.K. Chua, Geometry dependence of microstructure and microhardness for selective electron beam-melted Ti–6Al–4V parts, Virtual Phys. Prototyp. 11 (2016) 183–191.
[27] P. Wang, X. Tan, M.L.S. Nai, S.B. Tor, J. Wei, Spatial and geometrical-based characterization of microstructure and microhardness for an electron beam melted Ti-6Al-4V component, Mater. Des. 95 (2016) 287–295.
[28] S.M.J. Razavi, P. Ferro, F. Berto, Fatigue assessment of Ti–6Al–4V circular notched specimens produced by selective laser melting, Metals 7 (2017) 291.
[29] M. Kahlin, H. Ansell, J.J. Moverare, Fatigue behaviour of notched additive manufactured Ti6Al4V with as-built surfaces, Int. J. Fatigue 101 (2017) 51–60.
[30] S.M.J. Razavi, P. Ferro, F. Berto, J. Torgersen, Fatigue strength of blunt V-notched specimens produced by selective laser melting of Ti-6Al-4V, Theor. Appl. Fract. Mech. 97 (2018) 376–384.
[31] M. Benedetti, C. Santus, Notch fatigue and crack growth resistance of Ti-6Al-4V ELI additively manufactured via selective laser melting: a critical distance approach to defect sensitivity, Int. J. Fatigue 121 (2019) 281–292.
[32] M. Benedetti, C. Santus, F. Berto, Inverse determination of the fatigue strain energy density control radius forconventionally and additively manufactured rounded V-notches, Int. J. Fatigue 126 (2019) 306–318.
[33] D.A. Macdonald, The application of focus variation microscopy for lithic use-wear quantification, J. Archaeol. Sci. 48 (2014) 26–33.
[34] J. Pegues, M. Roach, R.S. Williamson, N. Shamsaei, Surface roughness effects on the fatigue strength of additively manufactured Ti-6Al-4V, Int. J. Fatigue 116 (2018) 543–552.
[35] N. Kashaev, M. Horstmann, V. Ventzke, S. Riekehr, N. Huber, Comparative study of mechanical properties using standard and micro-specimens of base materials Inconel 625, Inconel 718 and Ti-6Al-4V, J. Mater. Res. Technol. 2 (2013) 43–47.
[36] Y.Z. Wang, H.S. Ding, R.R. Chen, J.J. Guo, H.Z. Fu, Dependency of microstructure and microhardness on withdrawal rate of Ti-43Al-2Cr-2Nb alloy prepared by electromagnetic cold crucible directional solidification, Res. Dev. 13 (4) (2016) 289–293.
[37] Razavi S.M.J., Bordonaro G., Ferro P., Torgersen J., Berto F. Porosity effect on tensile behavior of Ti-6Al-4V specimens produced by laser engineered net shaping technology. Proc. Inst. Mech. Eng. Part C J. Mech. Eng. Sci. (in press) (DOI:https://doi.org/10.1177/0954406218813384).
[38] B. Wysocki, P. Maj, R. Sitek, J. Buhagiar, K.J. Kurzydlowski, W. Swieszkowski, Laser and electron beam additive manufacturing methods of fabricating titanium bone implants, Appl. Sci. 7 (2017) 657.
[39] Y. Zhai, H. Galarraga, D.A. Lados, Microstructure, static properties, and fatigue crack growth mechanisms in Ti-6Al-4V fabricated by additive manufacturing: LENS and EBM, Eng. Fail. Anal. 69 (2016) 3–14.
[40] X. Zhao, S. Li, M. Zhang, Y. Liu, T.B. Sercombe, S. Wang, Y. Hao, R. Yang, L.E. Murr, Comparison of themicrostructures andmechanical properties of Ti–6Al–4V fabricated by selective laser melting and electron beam melting, Mater. Des. 95 (2016) 21–31.
[41] V. Chastand, P. Quaegebeur, W. Maia, E. Charkaluk, Comparative study of fatigue properties of Ti-6Al-4V specimens built by electron beam melting (EBM) and selective laser melting (SLM), Mater. Charact. 143 (2018) 76–81.
[42] C. de Formanoir, S. Michotte, O. Rigo, L. Germain, S. Godet, Electron beam melted Ti–6Al–4V: microstructure, texture and mechanical behavior of the as-built and heat-treated material, Mater. Sci. Eng. A 652 (2016) 105–119.
[43] J. Dzugan, M. Seifi, R. Prochazka, M. Rund, P. Podany, P. Konopik, J.J. Lewandowski, Effects of thickness and orientation on the small scale fracture behaviour of additively manufactured Ti-6Al-4V, Mater. Charact. 143 (2018) 94–109.
[44] Ti6Al4V Titanium Alloy - Arcam AB, http://www.arcam.com/wp-content/uploads/Arcam-Ti6Al4V-Titanium-Alloy.pdf [Accessed 30 April 2020].
[45] J. Alcisto, A. Enriquez, H. Garcia, S. Hinkson, T. Steelman, E. Silverman, P. Valdovino, H. Gigerenzer, J. Foyos, J. Ogren, J. Dorey, K. Karg, T. McDonald, O.S. Es-Said, Tensile properties and microstructures of laser-formed Ti–6Al–4V, J. Mater. Eng. Perform. 20 (2) (2011) 203–212.
[46] T. Vilaro, C. Colin, J.D. Bartout, As-fabricated and heat-treated microstructures of the Ti-6Al-4V alloy processed by selective laser melting, Metall Mater Trans A 42 (10) (2011) 3190–3199.
[47] M. Koike, P. Greer, K. Owen, G. Lilly, L.E. Murr, S.M. Gaytan, E. Martinez, T. Okabe, Evaluation of titanium alloys fabricated using rapid prototyping technologies-electron beam melting and laser beam melting, Materials 4 (10) (2011) 1776–1792.
[48] B. Vrancken, L. Thijs, J.P. Kruth, J. Van Humbeeck, Heat treatment of Ti6Al4V produced by selective laser melting: microstructure and mechanical properties, J. Alloys Compd. 541 (2012) 177–185.
[49] S. Baragetti, R. Gerosa, Notch effect and fatigue performance of Ti-6Al-4V sheets in saline environment, Mater. Perform. Charact. 3 (2014) 1–9.
[50] S. Baragetti, Notch corrosion fatigue behavior of Ti-6Al-4V, Materials 7 (2014) 4349–4366.
[51] S. Baragetti, F. Villa, Quasi-static behavior of notched Ti-6Al-4V specimens in water- methanol solution, Corros Rev 33 (2015) 477–485.
[52] S. Baragetti, E.V. Arcieri, Corrosion fatigue behavior of Ti6Al4V alloy: chemical and mechanical driving forces, Int. J. Fatigue 112 (2018) 301–307.
[53] L.E. Murr, E.V. Esquivel, S.A. Quinones, S.M. Gaytan, M.I. Lopez, E.Y. Martinez, F. Medina, D.H. Hernadez, E.Y. Martinez, J.L. Martinez, S.W. Stafford, D.K. Brown, T. Hoppe, W. Meyers, U. Lindhe, R.B. Wicker, Microstructures and mechanical properties of electron beam-rapid manufactured Ti-6Al-4V biomedical prototypes compared to wrought Ti-6Al-4V, Mater. Charact. 60 (2009) 96–105.
[54] H.Y. Wana, G.F. Chen, C.P. Li, X.B. Qi, G.P. Zhang, Data-driven evaluation of fatigue performance of additive manufactured parts using miniature specimens, J. Mater. Sci. Technol. Res. 35 (2019) 1137–1146.
[55] A. Yadollahi, N. Shamsaei, Additive manufacturing of fatigue resistant materials: challenges and opportunities, Int. J. Fatigue 98 (2017) 14–31.
[56] Y. Zhai, D.A. Lados, E.J. Brown, G.N. Vigilante, Fatigue crack growth behavior and microstructural mechanisms in Ti-6Al-4V manufactured by laser engineered net shaping, Int. J. Fatigue 93 (2016) 51–63.
[57] S. Hosseini, Fatigue of Ti-6Al-4V, Biomed Eng-Tech. Appl Med, IntechOpen, 2012, pp. 75–92.
[58] P. Li, D.H. Warner, A. Fatemi, N. Phan, Critical assessment of the fatigue performance of additively manufactured Ti–6Al–4V and perspective for future research, Int. J. Fatigue 85 (2016) 130–143.
[59] R.J. Morrissey, D.L. McDowell, T. Nicholas, Frequency and stress ratio effects in high cycle fatigue of Ti-6Al-4V, Int. J. Fatigue 21 (1999) 679–685.
[60] S. Hidetoshi, S. Hiroyuki, T. Kiyotaka, Surface crack initiation in pure titanium under various stress frequencies, Eng. Fract. Mech. 49 (1994) 317–321.
[61] M. Karl, R. Kelly, Influence of loading frequency on implant failure under cyclic fatigue conditions, Dent. Mater. 25 (2009) 1426–1432.
[62] A.H. Chern, P. Nandwana, T. Yuan, M.M. Kirka, R.R. Dehoff, P.K. Liaw, C.E. Duty, A review on the fatigue behavior of Ti-6Al-4V fabricated by electron beam melting additive manufacturing, Int. J. Fatigue 119 (2019) 173–184.
[63] K.S. Chan, M. Koike, R.L. Mason, T. Okabe, Fatigue life of titanium alloys fabricated by additive layer manufacturing techniques for dental implants, Metall. Mater. Trans. A 44 (2013) 1010–1022.
[64] K.S. Chan, Characterization and analysis of surface notches on Ti-alloy plates fabricated by additive manufacturing techniques, Surf. Topogr. Metrol Prop. 3 (2015) 044006.
[65] W.J. Sames, F.A. List, S. Pannala, R.R. Dehoff, S.S. Babu, The metallurgy and processing science of metal additive manufacturing, Int. Mater. Rev. 61 (2016) 315–360.
[66] D.H. Abdeen, B.R. Palmer, Effect of processing parameters of electron beam melting machine on properties of Ti-6Al-4V parts, Rapid Prototyp. J. 22 (2016) 609–620.
[67] A. Mohammad, M.K. Mohammed, A.M. Alahmari, Effect of laser ablation parameters on surface improvement of electron beam melted parts, Int. J. Adv. Manuf. Technol. 87 (2016) 1033–1044.
[68] P. Wang, W.J. Sin, M.L.S. Nai, J. Wei, Effects of processing parameters on surface roughness of additive manufactured Ti-6Al-4V via electron beam melting, Materials 10 (2017) 1121.
[69] N. Ahmed, B.M. Abdo, S. Darwish, K. Moiduddin, S. Pervaiz, A.M. Alahmari, M. Naveed, Electron beam melting of titanium alloy and surface finish improvement through rotary ultrasonic machining, Int. J. Adv. Manuf. Technol. 92 (2017) 3349–3361.
[70] Y.Y. Sun, S. Gulizia, C.H. Oh, D. Fraser, M. Leary, Y.F. Yang, M. Qian, The influence of as-Built surface conditions on mechanical properties of Ti-6Al-4V additively manufactured by selective electron beam melting, JOM 68 (2016) 791–798.
[71] S.M.J. Razavi, F. Berto, Directed energy deposition versus wrought Ti-6Al-4V: a comparison of microstructure, fatigue behavior, and notch sensitivity, Adv. Eng. Mater. 21 (8) (2019) 1900220.
[72] G. Meneghetti, D. Rigon, C. Gennari, An analysis of defects influence on axial fatigue strength of maraging steelspecimens produced by additive manufacturing, Int. J. Fatigue 118 (2019) 54–64, https://doi.org/10.1016/j.ijfatigue.2018.08.034.
[73] D. Rigon, G. Meneghetti, An engineering estimation of fatigue thresholds from a microstructural size and Vickers hardness: application to wrought and additively manufactured metals, Int. J. Fatigue 139 (2020) 105796, , https://doi.org/10.1016/j.ijfatigue.2020.105796.
[74] N. Hrabe, T. Gnäupel-Herold, T. Quinn, Fatigue properties of a titanium alloy (Ti–6Al–4V) fabricated via electron beam melting (EBM): effects of internal defects and residual stress, Int. J. Fatigue 94 (2017) 202–210.
[75] D. Greitemeier, F. Palm, F. Syassen, T. Melz, Fatigue performance of additive manufactured TiAl6V4 using electronand laser beam melting, Int. J. Fatigue 94 (2017) 211–217.
[76] X. Shui, K. Yamanaka, M. Mori, Y. Negata, K. Kurita, A. Chiba, Effects of post-processing on cyclic fatigue response of a titanium alloy additively manufactured by electron beam melting, Mater. Sci. Eng. A 680 (2017) 239–248.